

Article

One-Step Production of Highly Selective Ethylbenzene and Propylbenzene from Benzene and Carbon Dioxide via Coupling Reaction

Tianyun Wang¹, Yingjie Guan¹, Haidan Wu¹, Zhaojie Su¹, Jianguo Zhuang¹, Siyan Yan¹, Xuedong Zhu^{1,*} and Fan Yang^{2,*}

¹ Engineering Research Center of Large Scale Reactor Engineering and Technology, Ministry of Education, East China University of Science and Technology, Shanghai 200237, China; y30210060@mail.ecust.edu.cn (T.W.); y21220003@mail.ecust.edu.cn (Y.G.); haidan_wu@163.com (H.W.); y21210009@mail.ecust.edu.cn (Z.S.); jianguo18617@163.com (J.Z.); yansiyang001@163.com (S.Y.)

² State Key Laboratory of Green Chemical Engineering and Industrial Catalysis, Sinopec Shanghai Research Institute of Petrochemical Technology Co., Ltd., Shanghai 201208, China

* Correspondence: xdzhu@ecust.edu.cn (X.Z.); yangfan.sshy@sinopec.com (F.Y.); Tel.: +86-18917102386 (X.Z.)

Abstract: Utilizing carbon dioxide as a carbon source for the synthesis of olefins and aromatics has emerged as one of the most practical methods for CO₂ reduction. In this study, an improved selectivity of 85% for targeting products (ethylbenzene and propylbenzene) is achieved with a benzene conversion of 16.8% by coupling the hydrogenation of carbon dioxide to olefins over the bifunctional catalyst “Oxide-Zeolite” (OX-ZEO) and the alkylation of benzene with olefins over ZSM-5. In addition to investigating the influence of SAPO-34 and ZSM-5 zeolite acidity on product distribution, catalyst deactivation due to coke formation is addressed by modifying both molecular sieves to be hierarchical to extend the catalyst lifespan. Even after 100 h of operation at 400 °C, the catalysts maintained over 80% selectivity towards the target products, with benzene conversion over 14.2%. Furthermore, the pathway of propylbenzene formation is demonstrated through simple experimental design, revealing that the surface Brønsted acid sites of SAPO-34 serve as its primary formation sites. This provides a novel perspective for further investigation of the reaction network.

Keywords: dual-bed catalyst system; CO₂ hydrogenation; bifunctional catalysts



Citation: Wang, T.; Guan, Y.; Wu, H.; Su, Z.; Zhuang, J.; Yan, S.; Zhu, X.; Yang, F. One-Step Production of Highly Selective Ethylbenzene and Propylbenzene from Benzene and Carbon Dioxide via Coupling Reaction. *Catalysts* **2024**, *14*, 288. <https://doi.org/10.3390/catal14050288>

Academic Editor: Adriana Maria da Silva

Received: 2 April 2024

Revised: 17 April 2024

Accepted: 22 April 2024

Published: 24 April 2024



Copyright: © 2024 by the authors. Licensee MDPI, Basel, Switzerland. This article is an open access article distributed under the terms and conditions of the Creative Commons Attribution (CC BY) license (<https://creativecommons.org/licenses/by/4.0/>).

1. Introduction

The hazards caused by the severe emission of carbon dioxide, such as ocean acidification and climate change, have become increasingly recognized [1,2]. At the same time, there is a growing understanding that carbon dioxide can serve as a benign carbon source for catalytic conversion into value-added fuels and chemicals [3–6]. This approach not only contributes to carbon dioxide emission reduction but also offers significant opportunities for employing carbon dioxide in the synthesis of olefins [7,8] and aromatics [9,10] as alternative strategies for mitigating emissions and developing cost-effective production routes for valuable chemicals.

Carbon dioxide catalytic conversion is a promising technology, which is currently focused on thermal catalysis [11], photocatalysis [12], electrocatalysis [13], etc. Photocatalysis, which can use energetic charge carriers (and the heat) to selectively drive a reaction toward a particular product along with the lowering of activation energy and allow for the discovery of novel and selective reaction pathways that were not possible in thermal catalysis [14], has been widely studied in various fields, such as the photocatalytic oxidation of BTEX over TiO₂-based catalysts [15,16] and CO₂ over cuprous oxide cubic particles. Especially, submicrometer cuprous oxide (Cu₂O) cubic particles, which can exhibit strong electric and magnetic Mie resonances, are of great significance in improving the catalytic

activity of metal oxide photocatalysts; the dielectric resonance-enhanced photocatalysis opens a new avenue for solar light harvesting and photocatalysis [17,18]. Researchers delve into the charge carrier dynamics of Cu_2O nanoparticles, which offer links to scattering and photocarrier dynamics in real photocatalysts and provide a recipe for the accurate quantification of the photocarrier dynamics [19]. However, the field of photocatalytic CO_2 is still on the verge of exploring and understanding the mechanisms of various catalytic reactions due to its high energy input, low yield, and poor stability.

On the other hand, aromatics, such as ethylbenzene and propylbenzene, serve as crucial organic raw materials extensively utilized across various industries, including chemical production and healthcare [20,21]. The main use of ethylbenzene is in the petrochemical industry as an intermediate for the production of styrene, which is further utilized to manufacture styrene-butadiene rubber, polystyrene, and expanded polystyrene [22,23]. Propylbenzene, conversely, finds widespread use as a solvent and in the printing and dyeing industry. The current industrial processes for producing propylbenzene are characterized by high consumption, time-intensiveness, substantial energy requirements, and significant wastewater emissions. The production methodology for ethylbenzene involves the alkylation of petroleum-based benzene, with ethylene produced from the cracking of naphtha, entailing high raw material costs, stringent catalyst lifespan requirements, and a heavy reliance on non-renewable petroleum resources [23–25]. Moreover, with the increasing market demand for ethylbenzene and the consequent shortage in the ethylene supply, these challenges have spurred researchers to explore new processes and the development of catalysts that are highly active, selective, and stable [26].

The structure–reactivity relationship is a hot topic in the field of catalysis, where tandem catalysis offers a promising solution for developing new production processes [27–30]. Reaction coupling integrates two or more reactions into a single reactor, conducting multiple unit operations and/or reaction processes simultaneously within one set of equipment. This approach enhances the coupling effect of the reactions, enabling precise control over the reaction steps. Consequently, it facilitates the high-selectivity synthesis of products with greater added value [31].

In essence, the process begins with the conversion of carbon dioxide into methanol/DME via metal/metal oxides, which is then swiftly transformed into lower olefins over the acid sites of SAPO-34, thereby activating CO_2 on a bifunctional “Oxide–Zeolite” (OX-ZEO) catalyst to synthesize lower olefins. This is followed by alkylation with benzene in the subsequent bed layer on the acid sites of ZSM-5, selectively producing ethylbenzene and propylbenzene, thus achieving the coupling of reactions and the direct synthesis of high-value chemicals from carbon dioxide in one step [32]. The one-step method for producing ethylbenzene and propylbenzene simplifies the process flow, reduces energy consumption, and eliminates the need for the separation, transportation, and storage of reaction intermediates. In this work, by adjusting the acidity of the zeolite and altering the catalyst combination, it is possible not only to enhance the selectivity for ethylbenzene and propylbenzene to 85% with a benzene conversion of 16.8% but also to further investigate the generation sites for propylbenzene within this work system. This provides new insights for advancing the industrialization of new production processes for highly selective ethylbenzene and propylbenzene.

2. Results and Discussion

2.1. Structure and Properties of $\text{Zn}_2\text{Ga}_{2-m}\text{Al}_m\text{O}_x$

The XRD patterns of Zn/Ga/Al oxides with different ratios prepared by the coprecipitation method are depicted in Figure 1. Previous studies have proven that bivalent and trivalent metal oxides can easily form a spinel structure, namely, the AB_2O_4 -type spinel [33]. Typical $\text{ZnGa}_2\text{O}_4/\text{ZnAl}_2\text{O}_4$ has a normal spinel crystal structure with an $\text{Fd}\bar{3}\text{m}$ space group. The normal spinel $\text{ZnGa}_2\text{O}_4/\text{ZnAl}_2\text{O}_4$ has tetrahedrally coordinated Zn sites (T_d) surrounded by four oxygen atoms and octahedrally coordinated Ga/Al sites (O_h) surrounded by six oxygen atoms. The 32 oxygen ions are C_{3v} sites arranged in a close-

packed cubic formation, leaving 64 tetrahedral (T_d) and 32 distorted (D_{3d}) sites [34,35], which makes the metal oxides have thermal stability, chemical stability, and mechanical heat resistance. In this study, the diffraction pattern of $ZnGaO_x$ shows the characteristic peaks of $ZnGa_2O_4$ at $2\theta = 18.44^\circ, 30.31^\circ, 35.70^\circ, 57.40^\circ,$ and 63.04° , which are attributed to the (111), (220), (311), (511), and (440) faces of the $ZnGa_2O_4$ spinel, respectively [36]. In particular, a peak at 31.73° denotes the (100) plane of ZnO. At Ga:Al = 3:1, 1:1, 1:3, the diffraction peaks of the spinel $ZnAl_2O_4$ (220), (311), and (422) planes appear at $2\theta = 31.34^\circ, 36.93^\circ,$ and 55.79° , respectively [37], and the intensities gradually strengthen with the decrease in the Ga/Al ratio. In a nonstoichiometric spinel structure, excessive zinc can occupy the positions of aluminum. The radius of a Zn atom (134 pm) is smaller than that of an Al atom (143 pm), so the peaks that are characterized as a $ZnAl_2O_4$ spinel shift to higher angles according to Bragg's law [38–40], which can totally explain why the peak of the $ZnAl_2O_4$ spinel (220) face changes slightly from 31.34° to $31.86^\circ, 31.96^\circ,$ and 31.78° at Ga:Al = 3:1, 1:1, and 1:3.

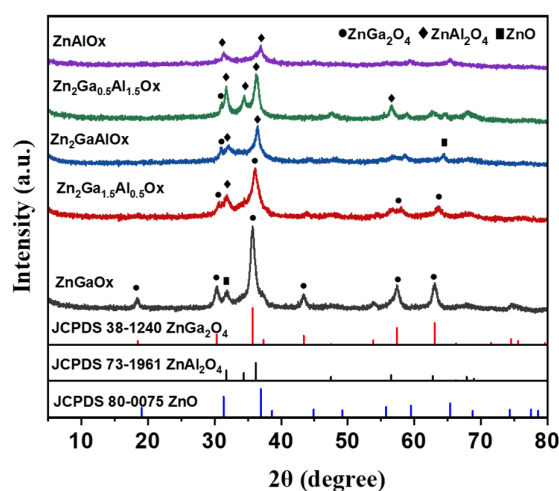


Figure 1. XRD patterns of Zn/Ga/Al oxides.

The TEM images of $ZnAlO_x$, $ZnGaO_x$, and $Zn_2Ga_{0.5}Al_{1.5}O_x$ are displayed in Figure S1. To investigate the impact of tri-elemental metal doping on the particle size distribution and surface morphology, we employed Transmission Electron Microscopy (TEM) to meticulously examine the three metal oxide samples. The mean size of $ZnGaO_x$ particles estimated from the TEM image was 22.5 nm, with a relatively narrow distribution (Figure S1a), displaying characteristic ZnO and spinel phases, which is corroborated by the X-ray Diffraction (XRD) results. The $ZnAlO_x$ samples were primarily composed of particles with dimensions around 4 nm and 15 nm, leading to a significant discrepancy in particle sizes. Meanwhile, the synthesized $Zn_2Ga_{0.5}Al_{1.5}O_x$ oxides show a remarkably narrow size distribution, confined within the range of 4–10 nm, and an average particle size of 5.5 nm, indicating that the addition of the three metals facilitates the dispersion of the particles as well as the reduction in the particle size. Morphologically, $Zn_2Ga_{0.5}Al_{1.5}O_x$ particles primarily exhibit a spinel structure without the appearance of any additional phases.

The textural properties of Zn/Ga/Al oxides are shown in Table 1. The specific surface area of the metal catalysts showed a volcanic trend with increasing Al content, and both the pore size and total pore volume decreased with a decreasing Ga/Al ratio, with a twofold difference.

To evaluate the electron structure and oxidation states of Zn, Al, Ga, and O in the ternary metal oxide system, X-ray Photoelectron Spectroscopy (XPS) characterization was conducted on individual samples (Figure 2). The Zn 2p XPS spectrum is shown in Figure 2a, where there are two peaks with binding energies (BEs) of 1021.22 eV and 1044.28 eV, attributed to the Zn 2p_{1/2} and 2p_{3/2} spin-orbit splitting peaks, originating from the ZnO or Zn/Ga/Al oxides, respectively [41]. There is no significant difference in the

Zn 2p peaks between all samples, suggesting that the Zn species have the same electronic properties, and the energy difference between the peaks is 23.06 eV [42], proving that the oxidation state of Zn is Zn^{2+} . Similarly, the high-resolution XPS spectrum of Al 2p is shown in Figure 2b, which only shows a single peak at 74.02 eV, and the oxidation state of Al can be determined as 3+; these Al^{3+} cations are bonded to oxygen as Al-O [43]. There is no obvious difference in the Al 2p peaks between the samples, suggesting that all of them have the same electronic structure.

Table 1. Textural properties and bulk compositions of the metal catalysts.

Sample	$S_{BET}/(m^2 \cdot g^{-1})$	$D_{pore}/(nm)$	$V_{total}/(cm^3 \cdot g^{-1})$
ZnGaO _x	63	171	0.27
Zn ₂ Ga _{1.5} Al _{0.5} O _x	70	136	0.24
Zn ₂ GaAlO _x	92	137	0.24
Zn ₂ Ga _{0.5} Al _{1.5} O _x	53	104	0.18
ZnAlO _x	50	98	0.12

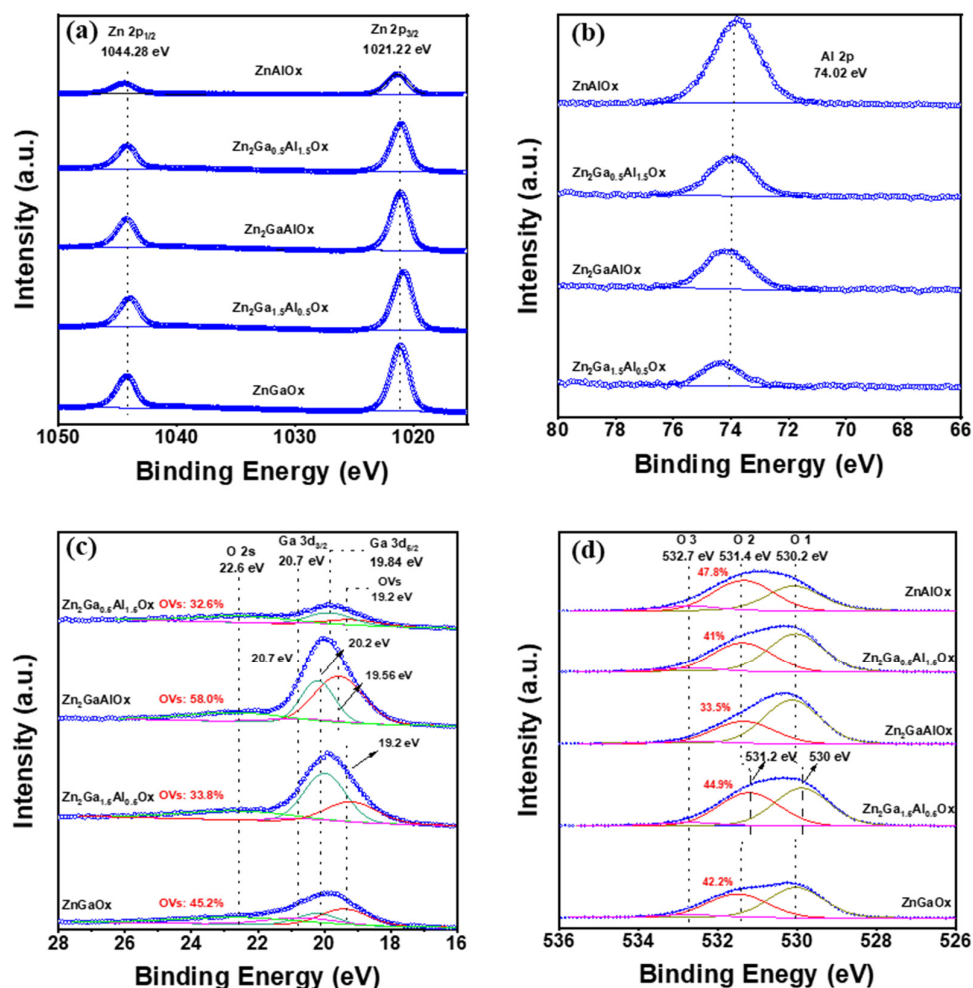


Figure 2. XPS spectra of (a) Zn 2p, (b) Al 2p, (c) Ga 3d, and (d) O 1s orbitals.

Figure 2c shows the Ga 3d XPS spectra. Generally, the Ga 3d orbital spectra can be further decomposed into two separate peaks, Ga 3d_{3/2} and Ga 3d_{5/2}, with BEs of 20.7 eV and 20.2 eV, respectively [44]. Since the whole spectrum is biased towards lower binding energies and oxygen vacancies (OVs) are reported to form on the surface of the samples due to defects or aberrations, an additional peak at the lower binding energy (19.2 eV) needs to be fitted to the curve to obtain a better fit [45,46]. OVs can be quantitatively described using the

following equation: $OVs\ concentrations = [S_{vacancies} / (S_{vacancies} + S_{Ga\ 3d3/2} + S_{Ga\ 3d5/2})]$ [47]. According to Figure 2c, the OVs content shows a “volcano” plot trend as the Ga/Al ratio decreases, with a large gap between different ratios, maxing out at Zn_2GaAlO_x (OVs = 58.0%). It has been reported that excess Zn tends to appear on the surface of Zn/Ga oxides and covers the surface of the oxide in an amorphous state [47]. According to XRD results, more non-stoichiometric Zn tends to be retained on the surface as an amorphous phase of ZnO when Ga/Al = 1. Thus, it is this part of the amorphous ZnO phase that produces the high oxygen vacancy concentration in Zn_2GaAlO_x . In addition, a broad peak at 22.6 eV is formed due to the partial overlap of Ga 3d and O 2s orbitals [48].

Figure 2d shows the XPS spectra of O 1s. Generally, O1, O2, and O3 refer to the three peaks at 530.2, 531.7, and 532.6 eV, respectively [49,50], and the O1 species are lattice oxygens from metal oxides or spinel phases. O2 and O3 are oxygen anions with less charge and chemisorbed oxygen from oxygen vacancies or surface defects, respectively [51,52]. There is a slight peak shift in O1 due to the different occupation of different lattice oxygens (the lattice energy of different lattice oxygens varies, e.g., the binding energies of the lattice oxygens of ZnO and Ga_2O_3 are 530.2 eV and 530.8 eV, respectively) in different samples. According to Figure 2d, as the Ga/Al ratio decreases, the oxygen vacancy O2 content decreases from 44.9% to 33.5% (Ga/Al = 1) and then increases to 47.8%. This indicates that the oxygen vacancy O2 in Zn_2GaAlO_x is significantly less than that in the other samples and the metal–metal interactions are weaker. According to the XRD results, it can be seen that there are two types of spinel phases, and various oxides exist in the sample at the same time when the Ga and Al doping amounts are different. When the phase occupancy is different, the nature of the oxygen vacancies in the sample, the electronic properties of the metal atoms, as well as the concentration and distribution of the oxygen vacancies also differ, which explains why the O XPS conclusions are not consistent with the Ga XPS conclusions [53]. Overall, the concentration of OVs is higher in the two-metal oxides than in the three-metal oxides, but in particular, the OVs are particularly high when Ga:Al = 3:1. Notably, the overall changes in O 1s binding energies are in opposition with those in Ga 3d, which indicates an electron transfer phenomenon from oxygen to gallium. According to previous studies, intermetallic oxide charge transfer processes affect the catalyst reactivity to some extent [54]. The interatomic charge transfer reduces the activation energy of the reaction, while the OVs provide CO_2 adsorption sites, which synergistically promote the sequential hydrogenation of CO_2 to methanol, thus accelerating the reaction rate [55].

2.2. Characterizations of SAPO-34 and ZSM-5

Figure S2a shows the XRD patterns of synthetic hierarchical SAPO-34 with different Si/Al ratios. With the increase in the Si/Al ratio, the intensities of the characteristic diffraction peaks of SAPO-34 molecular sieves at $2\theta = 18.44^\circ, 30.31^\circ, 35.70^\circ, 57.40^\circ,$ and 63.04° are gradually strengthened [56], indicating a gradual improvement in the crystallinity of the molecular sieves, reaching its peak at a Si/Al ratio of 0.2. Figure S2b,c shows the XRD patterns of commercial ZSM-5 and synthetic hierarchical ZSM-5. The diffraction peaks shown at $2\theta = 8^\circ\sim 10^\circ$ and $20^\circ\sim 25^\circ$ demonstrate that the hierarchical and commercial ZSM-5 exhibit a typical MFI structure (JCPDS 44-0003).

To further explore the morphological and microscopic features of the molecular sieves, Figure 3 shows the SEM images of the hierarchical SAPO-34 with different Si/Al ratios. According to Figure 3a–e, it is clear that with the increase in the Si/Al ratio, the crystallinity increases, while the morphology of the samples gradually changes from a lamellar structure to a standard cubic morphology. The lower the Si/Al ratio, the larger the particle size, the more uniform the particle size distribution, the more defects on the surface, and the rougher the surface, which aligns with the diminished intensity of characteristic peaks observed in the XRD spectrum of SAPO-34 at lower Si/Al ratios [57]. Commercial SAPO-34 exhibits an ortho tetrahedral structure with a very non-uniform particle size from 10 μm to 30 μm . Figure 3g,h shows the synthesized hierarchical ZSM-5 with Si/Al = 65, which is very well

distributed with a larger particle size and higher crystallinity, unlike the commercial one (Figure 3i).

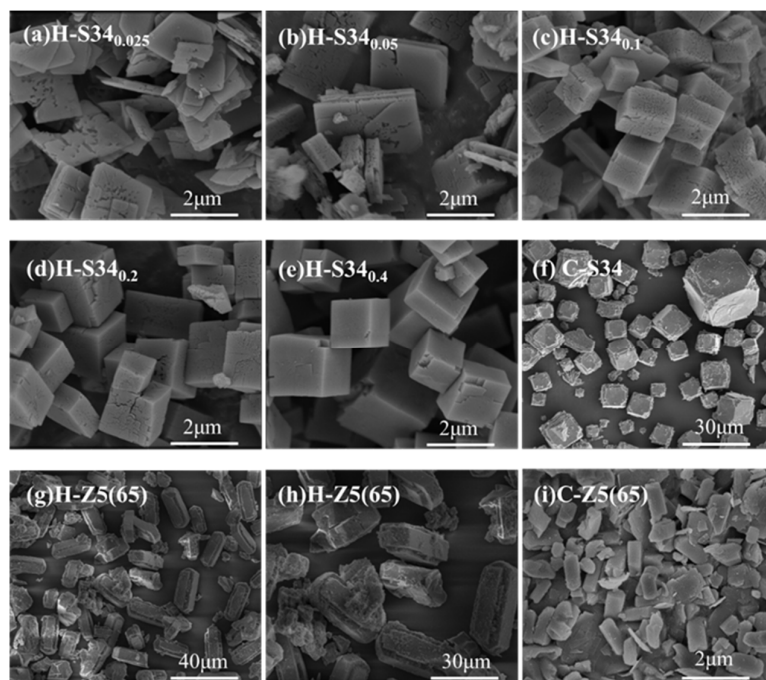


Figure 3. SEM micrographs of (a–e) hierarchical SAPO-34 with different Si/Al ratios, (f) commercial SAPO-34, (g,h) hierarchical ZSM-5, and (i) commercial ZSM-5.

Figure S4 shows the NH_3 temperature-programmed desorption (NH_3 -TPD) spectra of hierarchical SAPO-34 and ZSM-5. From Figure S4a, there is a low temperature desorption peak and a high temperature desorption peak at around 230 °C and 450 °C, respectively. Generally, the low-temperature desorption peak is attributed to the desorption of physisorbed NH_3 from the surface T-OH species (T = Si, Al, and P), indicating the presence of weak acid sites, while the high-temperature desorption peak is attributed to the desorption of NH_3 from the relatively strong Brønsted acid sites (BAS) or Lewis acid sites (LAS) [58,59]. It is observed that while there is no significant variance in the weak acid sites, the acid strength and acid density of strong acid exhibit a marked increase with the increase in the silica-to-alumina ratio (SARs), progressing from 385.6 $\mu\text{mol/g}$ to 764.85 $\mu\text{mol/g}$. Commercial SAPO-34 possesses more strong acid sites than the hierarchical SAPO-34 (986 $\mu\text{mol/g}$). According to Figure S4b, typically, the total acidity of ZSM-5 is usually identified as weak acid sites (<350 °C) and strong acid sites (>350 °C) [60]. For commercial ZSM-5, it is evident that the strong and weak acid sites as well as the acid densities gradually decrease with the increase in SARs. Compared with the commercial ZSM-5 with the same Si/Al ratio, the weak and strong acid peaks of the hierarchical ZSM-5 are slightly closer to the intermediate temperature, which indicates that there is a tendency for the acid sites of the hierarchical ZSM-5 to be shifted to the medium-strong level (Figure S4c).

In addition, in order to learn more about the acid properties, the IR spectra of SAPO-34 and ZSM-5 after the adsorption and desorption of ammonia and pyridine, respectively, are illustrated in Figure 4 and Figure S4. Before analyzing the NH_3 -IR spectra for SAPO-34, the substitution mechanism (SM) involved needs to be elucidated. Within the SAPO structure, the Brønsted acid sites (BAS) originate from charge-balancing protons generated by the substitution of silicon for the framework phosphorus or aluminum, and there are essentially two types of Si substitution mechanisms, namely, SM2 and SM3. In SM2, Si substitutes a P site of the framework, introducing a relatively weak BAS [61]. In SM3, a stronger acid site (as opposed to a single site) is formed when two adjacent Si atoms replace a pair (Al + P) to form a small Si island [62,63]. According to Figure 4, the BAS strength of SAPO-34

increases with increasing SAR, which is attributed to the fact that a majority of Si atoms are incorporated into SAPO-34, corroborating previous studies, and there appears to be no notable alteration in Lewis acid sites (LAS). The NH_3 -IR spectra at various temperatures reveal that the acid strength escalates with increasing SARs, and it is particularly significant that samples with SARs below 0.2 scarcely exhibit strong acid sites. The intensity and density of BAS in commercial ZSM-5 diminish markedly as the SAR increases, whereas the LAS remains unchanged. Meanwhile, in combination with the NH_3 -TPD results, it is evident that ZSM-5 zeolites with different SARs principally differ in terms of acid density and strength, exerting no substantial influence on acid properties (Figure S3).

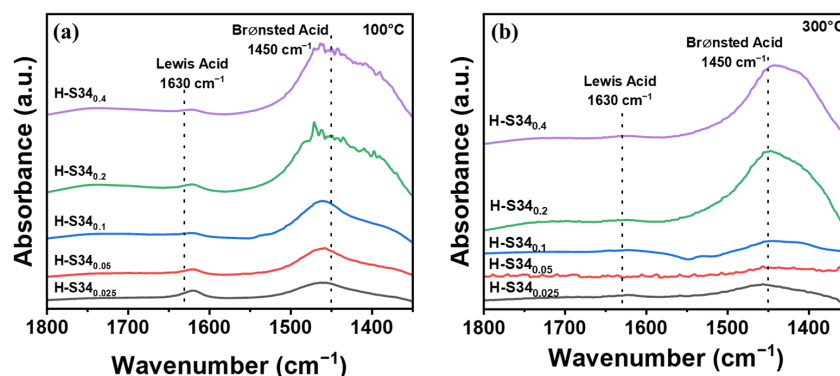


Figure 4. NH_3 -IR spectra of hierarchical SAPO-34 with different Si/Al ratios measured at (a) 100 °C and (b) 300 °C.

2.3. Catalytic Performance

2.3.1. Effects of Metal Oxides

Figures 5 and 6 present the catalytic performance of metal catalysts with different Ga/Al ratios. The liquid phase products (Figure 5) of the reaction predominantly consist of toluene, xylene, ethylbenzene, propylbenzene, and a minor fraction of C_{9+} . An analysis of the evaluation results reveals a distinct observation: the overall activity of the catalysts exhibits an improvement with the addition of either Ga or Al metals exclusively. Specifically, the benzene conversions of ZnGaO_x and ZnAlO_x are marginally superior to those of other catalysts, recorded at 9.4% and 8.2%, respectively. However, the increase in benzene conversion is accompanied by a higher selectivity for the side products, indicating that ternary metal catalysts demonstrate a greater selectivity towards the target products.

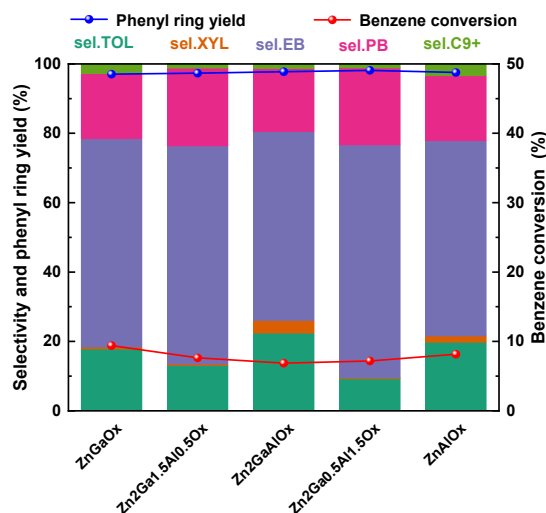


Figure 5. Conversions of benzene and composition of the liquid phase with different Zn/Ga/Al oxides. Reaction conditions: 400 °C, 3 MPa, $\text{H}_2:\text{CO}_2:\text{Benzene} = 12:4:1$, $\text{GHSV} = 22,500 \text{ mL} \cdot \text{g}_{\text{cat}}^{-1} \cdot \text{h}^{-1}$, $\text{WHSV} = 0.9 \text{ g}_{\text{benzene}} \cdot \text{g}_{\text{cat}}^{-1} \cdot \text{h}^{-1}$.

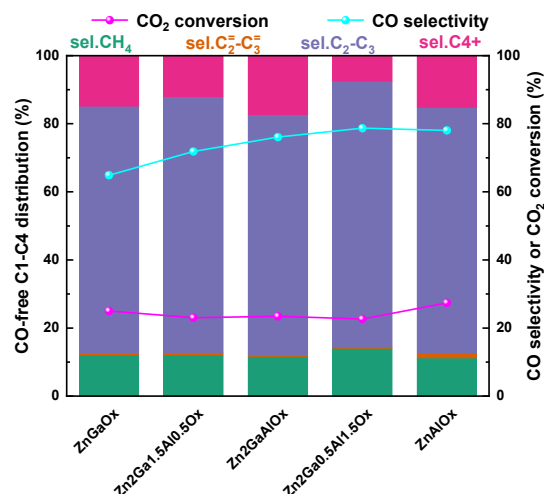


Figure 6. Conversions and traces of CO₂ with different Zn/Ga/Al oxides. Reaction conditions: 400 °C, 3 MPa, H₂:CO₂:Benzene = 12:4:1, GHSV = 22,500 mL·g_{cat}⁻¹·h⁻¹, WHSV = 0.9 g_{benzene}·g_{cat}⁻¹·h⁻¹.

Contrary to other ternary catalysts with different Ga/Al ratios, the Zn₂GaAlO_x catalyst exhibits a notably high selectivity for the side products toluene and xylene, reaching 26.1%, which is approximately 2.7 times higher than that observed for the Zn₂Ga_{0.5}Al_{1.5}O_x catalyst. The boost in xylene selectivity can be attributed to the further methylation reaction of toluene. It is worth noting that due to the similar boiling points of xylene and ethylbenzene, it is vital to minimize the selectivity of xylene to make it separate at an industrial scale conveniently. Focusing only on the selectivity, the Zn₂Ga_{0.5}Al_{1.5}O_x catalyst achieves the highest total selectivity for the target products ethylbenzene and propylbenzene, amounting to 89.2%.

In the gas phase, CO₂ conversions change in tandem with benzene conversions, with CO being the primary side product, accounting for approximately 60–80%, which is produced by a reverse-water-gas-shift (RWGS) reaction (Figure 6). The remaining products are mainly C₂–C₄₊ alkanes, which constitute 20–30% of the gas phase and are formed by the high-pressure hydrogenation of olefins in the upper layer of the reactor.

According to previous studies, textural properties such as the specific surface area of metal oxides are hardly decisive for the final reaction performance, and the specific surface area actually varies not by much for most Zn/Ga/Al oxides in Table 1 [64]. Instead, the activity and selectivity of the reaction can be safely attributed to the catalyst surface structure, which influences the catalytic performance mainly through OVs. The content of OVs determines the CO₂ adsorption capacity on the surface of the metal catalyst. In brief, the CO₂ adsorption capacity is determined by the moderately basic sites on the surface of the catalyst, which are the adsorption and activation sites for CO₂ hydrogenation and are related to the metal–oxygen pairs. An increase in the concentration of OVs inevitably leads to an increase in the number of metal–oxygen pairs, which leads to an increase in the number of CO₂ adsorption sites and a naturally high reactivity [65]. In addition, some DFT calculations have shown that oxygen vacancies contribute significantly to both the adsorption and activation of CO₂ by enhancing the adsorption energy of CO₂ and reducing the energy barrier of CO₂ dissociation, which demonstrates that the presence of oxygen vacancies promotes the activation of CO₂ kinetically. The lateral interaction of oxygen vacancies can generate divalent vacancies; once one of the two O atoms of CO₂ is inserted into the surface OVs, a bent CO₂⁻ intermediate is formed, which reduces the activation energy for the decomposition of CO₂ on divalent vacancies to almost half of that of a single isolated vacancy and further enhances the adsorption and activation of CO₂ on oxygen vacancies to increase the reaction rate [66,67]. This explains why the total selectivity of toluene and xylene is much higher with Ga/Al = 1 than with Ga/Al = 1:3 or 3:1. According to Ga XPS, the OVs of the catalyst with Ga/Al = 1 are almost twice

as high as other catalysts. Excessive oxygen vacancies in the metal catalyst for carbon dioxide activation and insufficient acid centers in SAPO-34 for methanol intermediate hydrogenation to olefins result in difficulties in continuous carbon chain growth reactions; intermediate species not consumed in situ enter the lower bed methylated with benzene at ZSM-5 to consequently form toluene. Therefore, combining the evaluation results with the catalyst characterization analysis, the OV's emerge as the primary determinant of catalytic performance, and the selective hydrogenation of CO₂ to low carbon olefins requires an optimal OV's concentration; otherwise, it is prone to exacerbate the benzyl alcohol alkylation side reaction to produce toluene and xylene.

2.3.2. Effects of the Catalyst Components Ratio

Before investigating the effect of the molecular sieves' silica-to-aluminum ratio (SAR) on the product distribution and reaction reactivity, the proportions of the components (three different catalysts mixed in one reactor) should be determined first. A series of comparative experiments were carried out with different mass ratios of metal oxides to SAPO-34 (Figure 7). The selectivity of toluene in the liquid phase products increased dramatically when the ratio of metal oxides to SAPO-34 was 5:1 and 1:5, which proved that if the ratio between the two was not moderate, the rate of methanol production from carbon dioxide on the metal oxides catalysts and the rate of the methanol to olefin (MTO) reaction in SAPO-34 could not match each other, and the side reaction of benzyl alcohol alkylation would be aggravated. The highest selectivity of the target products, 89.1%, was achieved when the metal oxides:SAPO-34 = 2:1.

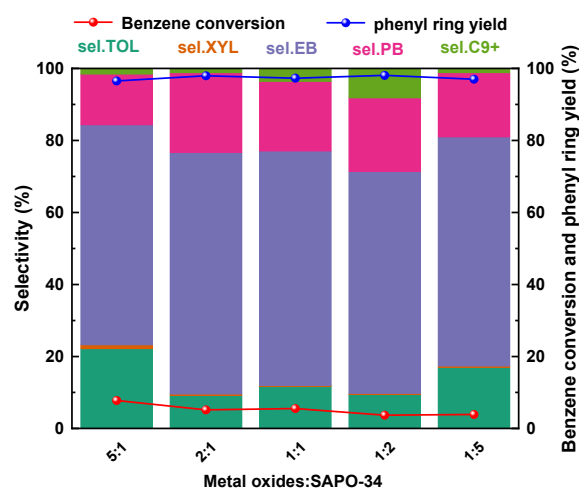


Figure 7. Conversions of benzene and composition of the liquid phase with different metal oxides to SAPO-34 ratios. Reaction conditions: 400 °C, 3 MPa, H₂:CO₂:Benzene = 12:4:1, GHSV = 22,500 mL·g_{cat}⁻¹·h⁻¹, WHSV = 0.9 g_{benzene}·g_{cat}⁻¹·h⁻¹.

2.3.3. Effects of SARs of SAPO-34

Figure 8 presents the catalytic performance of SAPO-34 with different Si/Al ratios. The results reveal a noteworthy correlation between the SAPO-34 SARs and product selectivity in the catalytic performance. It can be seen that the benzene conversions increase with increasing SARs, while the total selectivity of the target product shows a “volcano-shaped” trend as the SARs increase, peaking at Si/Al = 0.2 with a maximum value of 87%. In particular, the selectivity trends of ethylbenzene and propylbenzene diverge significantly, with ethylbenzene demonstrating a classic “volcano” curve and propylbenzene demonstrating an inverted “volcano” curve (Figure 9). This divergence not only highlights the influential role of the SARs of SAPO-34 on the liquid phase product distribution but also suggests a competitive interplay or distinct requirement for specific properties of SAPO-34 between these two target products.

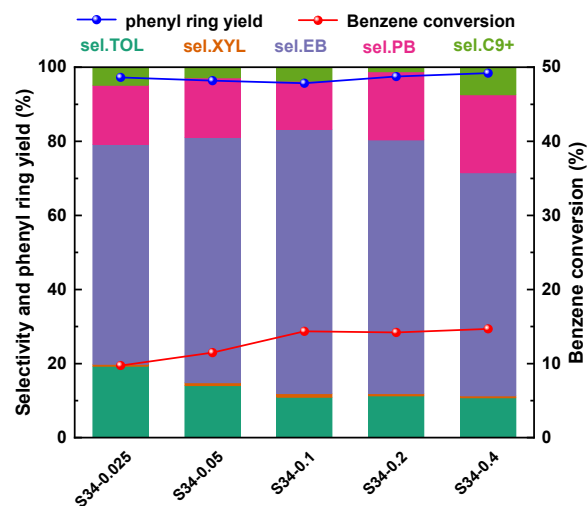


Figure 8. Conversions of benzene and composition of the liquid phase in SAPO-34 with different Si/Al ratios. Reaction conditions: 400 °C, 3 MPa, H₂:CO₂:Benzene = 12:4:1, GHSV = 22,500 mL·g_{cat}⁻¹·h⁻¹, WHSV = 0.9 g_{benzene}·g_{cat}⁻¹·h⁻¹.

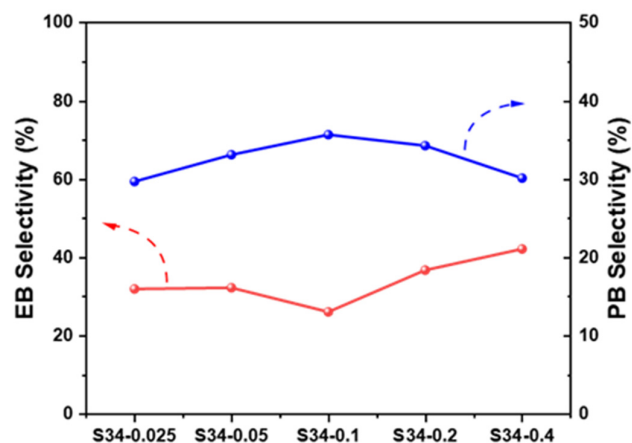


Figure 9. Selectivity of ethylbenzene and propylbenzene (EB and PB) in SAPO-34 with different Si/Al ratios.

The methanol to olefin reaction (MTO) is divided into the following three steps: (1) the formation of methoxy on the catalyst surface, (2) the formation of the first C-C olefinic bond, and (3) successive carbon growth. Of these, the first step is the rate-determining step, and the medium-strength Brønsted acid sites can provide stable surface methoxy into the CHA cage to produce olefins without causing olefin hydrogenation [68]. According to NH₃-TPD, the acid strength and acid density of BAS exhibit a marked increase with the increase in the silica-to-alumina ratio (SAR), progressing from 385.6 μmol/g to 764.85 μmol/g. Previous works have demonstrated that the acidity not only affects the lifetime but also influences the product selectivity. A higher acidic strength and concentration would promote the occurrence of side reactions, such as oligomerization, cyclization, and aromatization [69], which can explain the dramatic increase in C₉₊ at SAR = 0.4. The moderate acidity of the H-SAPO-34 could hinder the secondary transformations of light olefins, therefore resulting in higher C²⁼-C³⁼ selectivity [70], which also explains why the target products' selectivity reaches a maximum at SAR = 0.2. In summary, SAPO-34 acidity markedly influences the product distribution, ethylbenzene selectivity is higher when SAPO-34 weak acid predominates, and propylbenzene selectivity can be increased by improving SAPO-34 strong acid site density. Hence, to strategically modulate the product distribution with an aim of elevating ethylbenzene selectivity, an approach towards the further passivation of SAPO-34 surface acid strength is recommended.

2.3.4. Effects of SARs of ZSM-5

Figure 10 presents the catalytic performance of commercial ZSM-5 with different Si/Al ratios. At a low Si/Al ratio, the side products are predominantly low carbon aromatics, with a notable increase in xylene being the most apparent, probably due to the cracking reactions of ethylbenzene and propylbenzene caused by the strong acid strength of ZSM-5. In addition, toluene and xylene have lower diffusion resistances due to their smaller molecular sizes, facilitating their formation and diffusion processes. This dynamic significantly enhances the phenyl methylation reaction, leading to an optimal benzene conversion. As the SARs increase, the selectivity for propylbenzene significantly increases, whereas that for ethylbenzene noticeably decreases. Given these results, along with the observed increase in propylbenzene selectivity when SAPO-34 exhibits relative strong acidity, a reasonable hypothesis is proposed: the reaction between propylene and benzene requires only weak acid sites. In this work system, the main generation sites for propylbenzene are hypothesized to be the acid sites on the surface of SAPO-34, which will be experimentally validated later. According to this assumption, the propylbenzene produced on SAPO-34 is bound to be further cracked to produce smaller molecule by-products when it enters the ZSM-5 bed with strong acid (SAR = 18), which explains the tripling of toluene and xylene selectivity in the products compared to SAR = 150, and in addition, the side reaction of olefin hydrogenation is intensified at SAR = 18, further reducing the selectivity of the products.

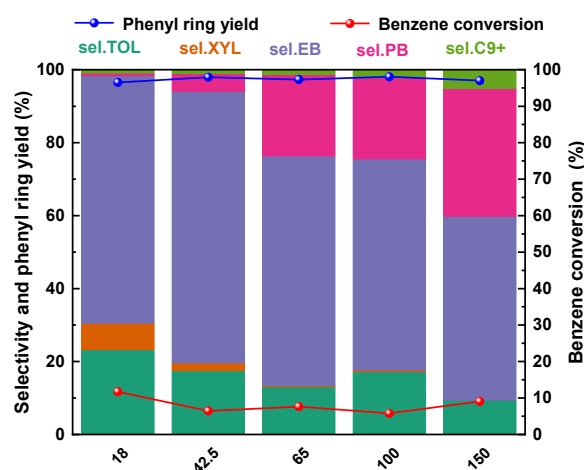


Figure 10. Conversions of benzene and composition of the liquid phase in ZSM-5 with different Si/Al ratios. Reaction conditions: 400 °C, 3 MPa, $H_2:CO_2:Benzenes = 12:4:1$, $GHSV = 22,500 mL \cdot g_{cat}^{-1} \cdot h^{-1}$, $WHSV = 0.9 g_{benzene} \cdot g_{cat}^{-1} \cdot h^{-1}$.

Furthermore, in order to eliminate the constraints of the reaction space, improve the effective utilization of active sites, and reduce the short catalyst life due to carbon deposition, hierarchical ZSM-5 with Si/Al = 65 was synthesized and introduced into the reaction (Figure 11). During the MTO reaction process or benzene alkylation, catalyst activity is very sensitive to carbon deposition and decreases rapidly as the carbon deposition increases. In general, carbon deposition can affect the activity of the catalyst in two ways: one is to cover the active sites of the molecular sieves or combine with the acid centers on the catalyst surface, ultimately leading to deactivation; the other is to deactivate the catalyst by blocking the pores on the surface, preventing the reactants from diffusing into the active sites or the products from diffusing out of the catalyst pores. It can be seen that the total selectivity of ethylbenzene and by-products (toluene, xylene) is improved through the hierarchical modification because of the smaller size and faster diffusion in the molecular sieve pores. The increase in benzene conversion is attributed to less carbon deposition and the enhanced mass transport of the hierarchical pore architecture. This modification resulted in a nearly threefold increase in benzene conversion to 16.8%, while maintaining target product selectivity at an impressive 85.1%.

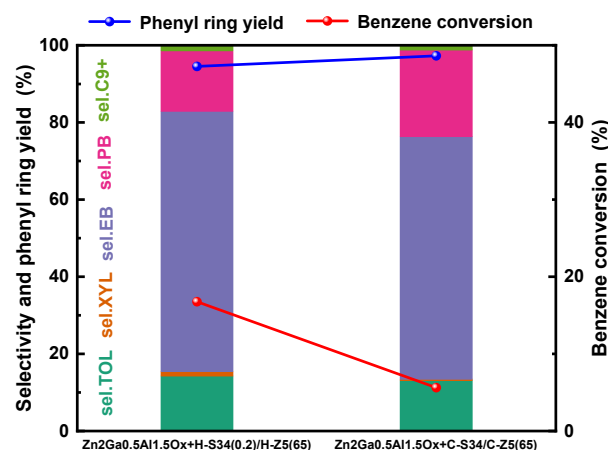


Figure 11. Comparison of commercial and hierarchical ZSM-5 (Si/Al = 65) in catalytic performance. Reaction conditions: 400 °C, 3 MPa, H₂:CO₂:Benzene = 12:4:1, GHSV = 22,500 mL·g_{cat}⁻¹·h⁻¹, WHSV = 0.9 g_{benzene}·g_{cat}⁻¹·h⁻¹.

2.3.5. Stability Tests

Meanwhile, stability is crucial for industrial catalysis; the catalyst stability was tested (Figure 12). After 100 h of the reaction at 400 °C, the benzene conversion remained around 15% and the target product selectivity remained above 80%, with only a slight decrease, indicating that the Zn₂Ga_{0.5}Al_{1.5}O_x+H-SAPO-34(0.2)/H-ZSM-5(65) catalyst was highly stable.

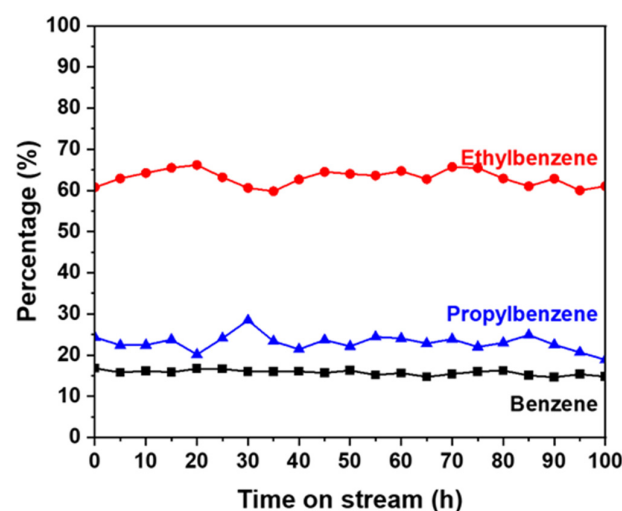


Figure 12. Stability of the Zn₂Ga_{0.5}Al_{1.5}O_x/H-S34(0.2) +H-Z5(65) catalyst in the reaction. Reaction condition: 400 °C, 3 MPa, H₂:CO₂:Benzene = 12:4:1, GHSV = 22,500 mL·g_{cat}⁻¹·h⁻¹, WHSV = 0.9 g_{benzene}·g_{cat}⁻¹·h⁻¹.

2.4. Investigation of Propylbenzene Formation Sites

To further validate the hypothesis that “the reaction between propylene and benzene requires only weak acid sites, with the main generation sites for propylbenzene being the surface acid sites of SAPO-34,” several straightforward experiments were conducted (Figure 13).

Initially, the lower layer of ZSM-5 was removed, allowing for the introduction of benzene and CO₂ into a singular bed of Zn₂Ga_{0.5}Al_{1.5}O_x+C-S34 to undergo a reaction. The observation of liquid phase products revealed the formation of toluene, ethylbenzene, and propylbenzene on the SAPO-34 surface (the pore size of SAPO-34 is smaller than the dynamic diameter of benzene; therefore, benzene can only alkylate with intermediates like methanol/DME on the surface), with propylbenzene notably dominating. This dominance unequivocally demonstrates that propylbenzene can indeed be synthesized on the acid

sites of the SAPO-34 surface and be preferentially formed on its surface. Subsequently, the experiment proceeded with a substitution of the reactants to benzene and propylene, while the catalysts were switched to equal masses of commercial SAPO-34, ZSM-5(18), and a combination of C-S34/C-Z5(18), adhering to the predetermined upper and lower mass ratio of 1:4. Observations from these three distinct systems yielded insightful results.

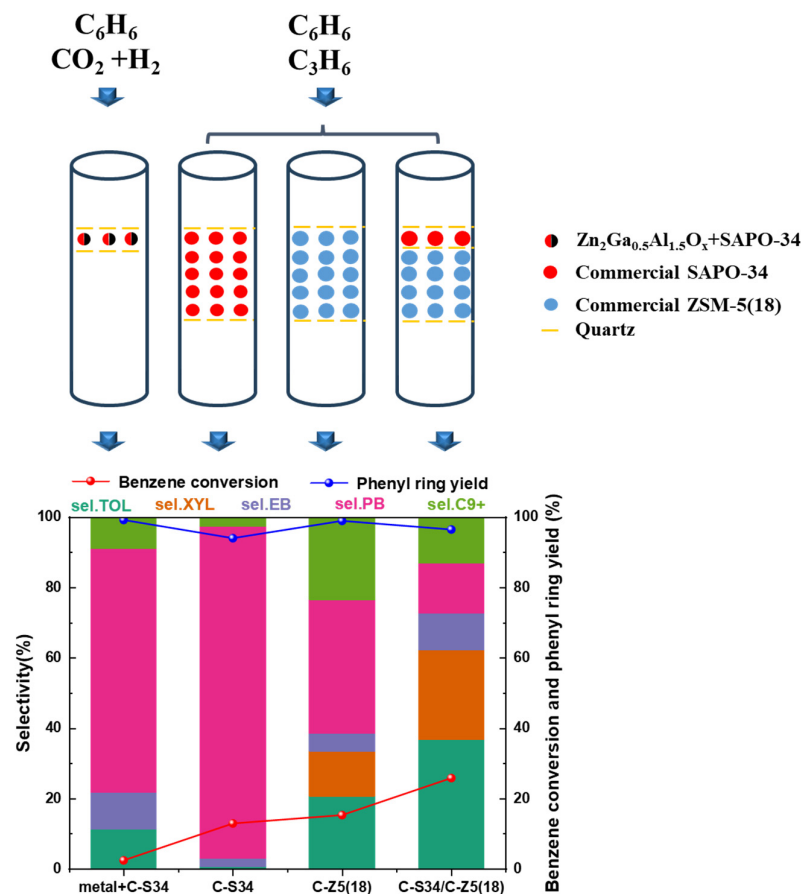
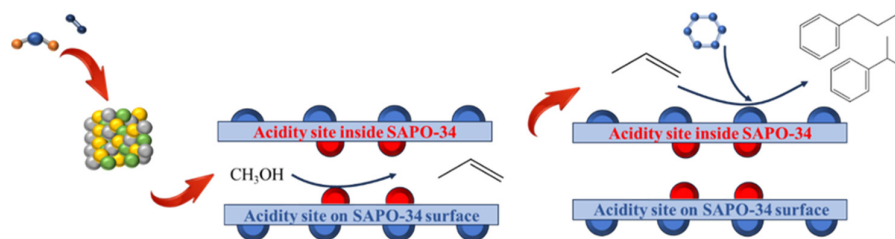


Figure 13. Effect of the series combination of catalysts on the product distribution and benzene conversion rate.

First, with SAPO-34 alone as the catalyst, propylbenzene accounted for over 90% of the products, further substantiating that the weak acid sites on the surface of SAPO-34 (in comparison to ZSM-5) are sufficient to support the formation of propylbenzene. Instead, when C-Z5(18) served as the only catalyst, a sharp increase in toluene and xylene was noted, indicating the instability and ease of the cracking of propylbenzene on strong acid sites. Upon employing the dual-bed system of C-S34/C-Z5(18), compared to the single C-Z5(18) layer, there was a further reduction in propylbenzene selectivity, with toluene and xylene comprising over 60% of the products. This outcome likely results from benzene and propylene almost completely reacting to form propylbenzene in the upper C-S34 layer, which then rapidly cracks into low carbon aromatics in the subsequent C-Z5 layer. Such a coupled reaction process enables a significant reduction in the selectivity for propylbenzene in the presence of a complete excess of propylene while concurrently doubling the benzene conversion.

The comprehensive analysis of the aforementioned experiments substantiates the following hypothesis: “The reaction between propylene and benzene requires only weak acid sites, with the primary generation sites for propylbenzene being the surface acid sites of SAPO-34 in this work system” (Scheme 1).



Scheme 1. Proposed generation sites for propylbenzene.

3. Materials and Methods

3.1. Source of Reagents

Samples were prepared with the following reagents. $\text{Zn}(\text{NO}_3)_2 \cdot 6\text{H}_2\text{O}$, $\text{Al}(\text{NO}_3)_3 \cdot 9\text{H}_2\text{O}$, benzene, and $(\text{NH}_4)_2\text{CO}_3$ were all purchased from China Shanghai Sinopharm Chemical Reagent Co, Ltd (Shanghai, China). $\text{Ga}(\text{NO}_3)_3 \cdot x\text{H}_2\text{O}$ was provided by Shanghai Aladdin Bio-Chem Technology Co., Ltd. (Shanghai, China). Silica sol ($\text{SiO}_2 \cdot \text{H}_2\text{O}$, 40%, Macklin, Shanghai, China), tetraethylorthosilicate (TEOS, $\text{SiO}_2 \geq 28.4\%$, Shanghai Titan Scientific Co., Ltd. Shanghai, China), phosphoric acid (H_3PO_4 , 85%, Shanghai Lingfeng Chemical Reagent Co., Ltd. Shanghai, China), and aluminum iso-propoxide ($\text{Al}(\text{O}i\text{-Pr})_3$, 98%, TCI, Shanghai, China) were used as Si, P, and Al sources, respectively. Triethylamine (TEA, 99%, Sinopharm Chemical Reagent Co., Ltd. Shanghai, China), tetraethylammonium hydroxide (TEAOH, 25wt%, Sinopharm Chemical Reagent Co., Ltd. Shanghai, China), tetrapropylammonium hydroxide (TPAOH, 40wt%, TCI, Shanghai, China), and hexadecyltrimethoxysilane (HTS, 98%, Sinopharm Chemical Reagent Co., Ltd. Shanghai, China) were employed as OSDAs. All reagents were used as received without further purifications. Commercial ZSM-5 (Si/Al = 18, 42.5, 65, 100, 150) was purchased from the Nankai University Catalyst Plant. Mixed gas containing CO_2 , H_2 , and nitrogen (N_2) was purchased from Air Liquide (China) Investment Co., Ltd. (Shanghai, China).

3.2. Synthesis

A series of Zn/Ga/Al oxides with different Zn:Ga:Al atomic ratios (2:2:0, 2:1.5:0.5, 2:1:1, 2:0.5:1.5, 2:0:2) were prepared through a coprecipitation method. $\text{Zn}(\text{NO}_3)_2 \cdot 6\text{H}_2\text{O}$, $\text{Al}(\text{NO}_3)_3 \cdot 9\text{H}_2\text{O}$, and $\text{Ga}(\text{NO}_3)_2 \cdot x\text{H}_2\text{O}$ were dissolved in deionized water to form a mixed salt solution. An aqueous solution of $(\text{NH}_4)_2\text{CO}_3$ was simultaneously added dropwise to the mentioned salt solution under continuous stirring at 30 °C. The obtained suspension was aged for 1 h at 30 °C, and then centrifuged and washed with deionized water until neutral. Finally, the precipitate was dried at 110 °C for 12 h and calcined in air at 450 °C for 6 h. The obtained catalyst was denoted as $\text{Zn}_a\text{Ga}_b\text{Al}_c\text{O}_x$, wherein a:b:c is the molar ratio of Zn:Ga:Al.

SAPO-34 (abbreviated as S34 in the text) was synthesized using a hydrothermal method. The precursor solutions were prepared according to the following molar composition: $x \text{SiO}_2 : 0.5 \text{Al}_2\text{O}_3 : 8 \text{TEA} : 0.8 \text{TEAOH} : 1 \text{P}_2\text{O}_5 : 70 \text{H}_2\text{O}$ ($x = 0.025, 0.05, 0.1, 0.2, 0.4$). DI water, aluminum iso-propoxide, and phosphoric acid were mixed and stirred at room temperature for 2 h. Silica sol was added, and the resulting mixture was kept stirring for 1 h, after which TEA and TEAOH were added to the solution. The mixture was stirred to obtain a uniform solution, transformed into a Teflon-lined stainless-steel autoclave, and crystallized at 200 °C for 24 h. The products were washed with deionized water several times and obtained by centrifugation, dried overnight at 80 °C, and calcined at 550 °C for 5 h. The samples synthesized with the Si/Al ratios of 0.025, 0.05, 0.1, 0.2, and 0.4 were named H-S34_{0.025}, H-S34_{0.05}, H-S34_{0.1}, H-S34_{0.2}, and H-S34_{0.4}, respectively. The commercial SAPO-34 was named C-S34.

ZSM-5 (abbreviated in the text as Z5, Si/Al = 65) molecular sieves were also prepared by hydrothermal synthesis. ZSM-5 precursor solutions were prepared according to the following molar composition: 130 $\text{SiO}_2 : 1 \text{Al}_2\text{O}_3 : 1.8 \text{TPAOH} : 0.5 \text{HTS} : 1250 \text{H}_2\text{O}$. Aluminum iso-propoxide was dissolved in DI water and stirred for 8 h. TPAOH and HTS were

added as OSDAs, and the solution was stirred until clarified. This was followed by the addition of TEOS, and the mixture went through further stirring for at least 6 h to afford a homogeneous mixture. The resulting solution was transferred into stainless steel autoclaves for the hydrothermal process at 180 °C for 72 h under tumbling (60 rpm). The products were washed with deionized water several times and obtained by centrifugation, dried overnight at 80 °C, and calcined at 550 °C for 5 h. The samples synthesized were named H-Z5(65). The commercial ZSM-5 was named Z5(Si/Al = 18, 42.5, 65, 100, 150).

The hybrid catalysts in the first bed were prepared by the physical mixing of SAPO-34 and different metal catalysts at an aimed mass ratio (SAPO-34:metal oxides = 1:2), respectively.

3.3. Catalyst Characterization

The crystal structure of all samples was measured by powder X-ray diffraction (XRD), which was operated on at 100 mA and 40 kV, employing Cu/K α ($\lambda = 1.5418 \text{ \AA}$) as the X-ray source. All samples were scanned at 40 kV and 40 mA in the range of 5–80°.

The surface morphology information and grain size of the samples were collected by Field-Emission scanning electron microscopy (FE-SEM) on a NOVA Nano SEM 450 (FEI, USA) setup with an accelerating voltage of 2.0 kV and transmission electron microscopy (TEM) on an FEI Tecnai G2 F30 transmission electron microscope operating at 300 kV.

The X-ray photoelectron spectroscopy (XPS) of Zn/Ga/Al oxides was carried out on a Thermo ESCALAB 250 instrument with monochromatic Al K α radiation (1486.6 eV) as the X-ray source, calibrated internally by the carbon deposit C(1s) (Eb = 284.6 eV).

NH₃-Temperature-programmed desorption (NH₃-TPD) was measured by a VODO VDSorb-91i instrument in a 10% NH₃-He mixture. The sample was placed in a U-shaped quartz tube, heated from room temperature to 500 °C at a rate of 20 °C/min in a helium atmosphere for 1 h to remove volatile impurities, and then cooled to room temperature to make contact with ammonia for 30 min. Prior to the record, the sample was purged by helium at 150 °C to sweep the additional NH₃. At last, the TCD signal was recorded by raising the temperature to 700 °C at a rate of 10 °C/min.

Nitrogen physisorption isotherms were performed on the Micrometrics 3Flex to detect specific surface properties and pore structures. Nitrogen adsorption was performed at −196 °C using liquid nitrogen as a coolant to obtain the corresponding adsorption–desorption isotherms. The specific surface area was calculated using the Brunauer–Emmett–Teller (BET) method. The surface areas and volumes of the micropores were determined by the t-plot method, and the total pore volume was estimated in terms of the relative pressure of 0.99.

The Fourier-transform infrared spectra of the adsorbed NH₃ (NH₃-IR) over SAPO-34 samples were acquired on a Nicolet-iS50 spectrometer. The samples were pressed into 30 mg discs, pretreated in the apparatus at 550 °C for 1 h to remove excess impurities and moisture, and then cooled to room temperature and maintained in ammonia for 30 min for full adsorption, after which the cell was purged with pure Ar for 20 min at 150 °C/200 °C, and the profiles were recorded, respectively.

Similarly, the 2,4,6-trimethylpyridine adsorption spectrum and infrared (IR) spectra of the pyridine adsorption at 200 °C were obtained by pretreating the wafer in the same procedure, and 2,4,6-trimethylpyridine/pyridine was introduced in the form of saturated vapor. To quantify the Lewis and Brønsted acid sites, the following Equations (1) and (2), reported by Emeis, were used [71]:

$$C_L = K_L A_{1450} = \frac{\pi}{IMEC_L} \left(\frac{r^2}{w} \right) A_{1450}, \quad (1)$$

$$C_B = K_B A_{1540} = \frac{\pi}{IMEC_B} \left(\frac{r^2}{w} \right) A_{1540}, \quad (2)$$

Herein, C_L and C_B correspond to the quantified concentrations of the Lewis and Brønsted acid sites; A_{1450} and A_{1540} are the corrected integral areas of peaks at 1450 and 1540 cm^{-1} in the curve of FT-IR spectra; K_L and K_B are the molar extinction coefficients for Lewis and Brønsted acid sites; IMEC_L and IMEC_B equal 2.22 and 1.67 $\text{cm}/\mu\text{mol}$ for Lewis and Brønsted acids, respectively; and w and r are the wafer weight and wafer radius of the disk.

3.4. Catalytic Tests

Since the different distances and spatial arrangements of the active centers between the three components (Zn/Ga/Al oxides, SAPO-34, and ZSM-5) significantly affect the distribution of the products, we have used the upper and lower beds in a tandem route for the catalytic reaction to make the reaction network simpler. All evaluations were performed in a high-pressure fixed bed reactor with 304 stainless steel tubing. Generally, 2 g catalysts with a particle size of 20–40 meshes were loaded into the upper and lower beds in a mass ratio of 1:4 (metal oxides + SAPO-34:ZSM-5), with a 2:1 mass ratio of the metal catalyst to SAPO-34 in the upper bed layer; the catalyst in each bed was mixed with double-dose quartz sand. The upper and lower beds were separated by 1 g of quartz, and the rest of the tube was also filled with quartz.

The catalyst was pre-reduced with hydrogen at 430 °C for 1 h and then cooled down to 400 °C. The reactant, where the molar ratio of $\text{H}_2:\text{CO}_2:\text{C}_6\text{H}_6$ was designed to be 12:4:1, with a pressure of 3.0 MPa, was introduced into the reactor to start the reaction. Unless specified, the reaction was performed at 400 °C and 3.0 MPa, with a gas hourly space velocity (GHSV) of 22,500 $\text{mL}\cdot\text{g}_{\text{cat}}^{-1}\cdot\text{h}^{-1}$ and a benzene weight hourly space velocity (WHSV) of 0.9 $\text{g}_{\text{benzene}}\cdot\text{g}_{\text{cat}}^{-1}\cdot\text{h}^{-1}$. The gas phase was introduced into an online chromatograph produced by Shimadzu using a TDX-02 packed column (2 m) connected to a TCD detector and a PLOT-Q capillary column (30 m) connected to an FID detector. After being cooled at room temperature through the cooling tank, the liquid products were analyzed using offline gas chromatography equipped with an FID detector connected to a DB-WAX capillary column (30 m).

4. Conclusions

A dual-bed layer system was used to couple the CO_2 hydrogenation to a low-carbon olefins reaction and the benzene alkylation with an olefin reaction to achieve highly selective hydrogenation. A comprehensive investigation was conducted into the effects of acidity in SAPO-34 and ZSM-5 molecular sieves on the products distribution; it is confirmed that ZSM-5 with low Si/Al ratios and strong Brønsted acid sites are more conducive to ethylbenzene production, while SAPO-34 with strong acidity favors propylbenzene generation. Based on the careful characterization of the catalysts, a hypothesis suggesting that propylbenzene is primarily generated at the surface acid sites of SAPO-34 is proposed and validated through straightforward comparative experiments. Hierarchical modifications were applied to the molecular sieves in order to improve the catalysts' lifespan, which resulted in a benzene conversion of 16.8% and a target product selectivity of 85%. Stability tests demonstrated that the catalysts could sustain operation under conditions of 400 °C and 3 MPa for over 100 h. This work advances the development of processes utilizing effective and stable catalysts for the conversion of carbon dioxide into high-value-added chemicals.

Supplementary Materials: The following supporting information can be downloaded at: <https://www.mdpi.com/article/10.3390/catal14050288/s1>, Figure S1: TEM images of (a) ZnGaOx; (b) ZnAlOx; (c) Zn₂Ga_{0.5}Al_{1.5}Ox; Figure S2: XRD patterns of (a) hierarchical SAPO-34, (b) commercial ZSM-5, and (c) comparison of commercial and hierarchical ZSM-5 (Si/Al = 65); Figure S3: NH₃-TPD patterns of (a) hierarchical SAPO-34 with different Si/Al ratios, (b) commercial ZSM-5 zeolites, and (c) comparison of commercial and hierarchical ZSM-5 (Si/Al = 65); Figure S4: IR spectra of commercial ZSM-5 with different Si/Al ratios measured at 200 °C (a) and 500 °C (b); comparison of commercial and hierarchical ZSM-5 (Si/Al = 65) (c); Figure S5: Nitrogen adsorption isotherms of SAPO-34 and ZSM-5; Table S1: Textural properties and surface compositions of SAPO-34 and ZSM-5.

Author Contributions: Conceptualization, T.W.; methodology, T.W. and F.Y.; validation, T.W. and Y.G.; formal analysis, T.W., S.Y. and J.Z.; investigation, T.W. and Z.S.; data curation, T.W. and H.W.; writing—original draft preparation, T.W.; writing—review and editing, T.W. and F.Y.; supervision, X.Z.; project administration, X.Z. All authors have read and agreed to the published version of the manuscript.

Funding: This research was funded by the National Natural Science Foundation of China, grant number 21776076, and the Fundamental Research Funds for the Central Universities, grant number JKA01211710.

Data Availability Statement: The data presented in this study are available in the article and Supplementary Materials.

Acknowledgments: The authors thank the Research Center of Analysis and Test of East China University of Science and Technology for the help with the characterizations.

Conflicts of Interest: Author Fan Yang was employed by the company State Key Laboratory of Green Chemical Engineering and Industrial Catalysis, Sinopec Shanghai Research Institute of Petrochemical Technology Co., Ltd. The remaining authors declare that the research was conducted in the absence of any commercial or financial relationships that could be construed as a potential conflict of interest.

References

1. Burkart, M.D.; Hazari, N.; Tway, C.L.; Zeitler, E.L. Opportunities and Challenges for Catalysis in Carbon Dioxide Utilization. *ACS Catal.* **2019**, *9*, 7937–7956. [[CrossRef](#)]
2. Porosoff, M.D.; Yan, B.; Chen, J.G. Catalytic reduction of CO₂ by H₂ for synthesis of CO, methanol and hydrocarbons: Challenges and opportunities. *Energy Environ. Sci.* **2016**, *9*, 62–73. [[CrossRef](#)]
3. Hepburn, C.; Adlen, E.; Beddington, J.; Carter, E.A.; Fuss, S.; Mac Dowell, N.; Minx, J.C.; Smith, P.; Williams, C.K. The technological and economic prospects for CO₂ utilization and removal. *Nature* **2019**, *575*, 87–97. [[CrossRef](#)] [[PubMed](#)]
4. Hu, J.; Yu, L.; Deng, J.; Wang, Y.; Cheng, K.; Ma, C.; Zhang, Q.; Wen, W.; Yu, S.; Pan, Y.; et al. Sulfur vacancy-rich MoS₂ as a catalyst for the hydrogenation of CO₂ to methanol. *Nat. Catal.* **2021**, *4*, 242–250. [[CrossRef](#)]
5. Zhou, C.; Shi, J.; Zhou, W.; Cheng, K.; Zhang, Q.; Kang, J.; Wang, Y. Highly Active ZnO-ZrO₂ Aerogels Integrated with H-ZSM-5 for Aromatics Synthesis from Carbon Dioxide. *ACS Catal.* **2020**, *10*, 302–310. [[CrossRef](#)]
6. Schieweck, B.G.; Jürling-Will, P.; Klankermayer, J. Structurally Versatile Ligand System for the Ruthenium Catalyzed One-Pot Hydrogenation of CO₂ to Methanol. *ACS Catal.* **2020**, *10*, 3890–3894. [[CrossRef](#)]
7. Li, Z.; Wang, J.; Qu, Y.; Liu, H.; Tang, C.; Miao, S.; Feng, Z.; An, H.; Li, C. Highly Selective Conversion of Carbon Dioxide to Lower Olefins. *ACS Catal.* **2017**, *7*, 8544–8548. [[CrossRef](#)]
8. Feng, L.; Guo, S.; Yu, Z.; Cheng, Y.; Ming, J.; Song, X.; Cao, Q.; Zhu, X.; Wang, G.; Xu, D.; et al. Developing Multifunctional Fe-Based Catalysts for the Direct Hydrogenation of CO₂ in Power Plant Flue Gas to Light Olefins. *Catalysts* **2024**, *14*, 204. [[CrossRef](#)]
9. Ni, Y.; Chen, Z.; Fu, Y.; Liu, Y.; Zhu, W.; Liu, Z. Selective conversion of CO₂ and H₂ into aromatics. *Nat. Commun.* **2018**, *9*, 3457. [[CrossRef](#)]
10. Fang, X.; Li, B.; Liu, H.; Xie, M.; Chen, Z.; Yang, L.; Han, J.; Zhu, W.; Liu, Z. High carbon utilization for CO₂ conversion with chloromethane to aromatics over acidic zeolite catalyst. *Chem Catal.* **2023**, *3*, 100689. [[CrossRef](#)]
11. Chen, Q.; Chen, D.; He, L. Production of ethylbenzene and propylbenzene from benzene alkylation using carbon dioxide. *Chem Catal.* **2022**, *2*, 930–932. [[CrossRef](#)]
12. Wang, Y.; Chen, E.; Tang, J. Insight on Reaction Pathways of Photocatalytic CO₂ Conversion. *ACS Catal.* **2022**, *12*, 7300–7316. [[CrossRef](#)] [[PubMed](#)]
13. Qu, J.; Cao, X.; Gao, L.; Li, J.; Li, L.; Xie, Y.; Zhao, Y.; Zhang, J.; Wu, M.; Liu, H. Electrochemical Carbon Dioxide Reduction to Ethylene: From Mechanistic Understanding to Catalyst Surface Engineering. *Nano-Micro Lett.* **2023**, *15*, 178. [[CrossRef](#)] [[PubMed](#)]
14. Verma, R.; Belgamwar, R.; Polshettiwar, V. Plasmonic Photocatalysis for CO₂ Conversion to Chemicals and Fuels. *ACS Mater. Lett.* **2021**, *3*, 574–598. [[CrossRef](#)]
15. Korologos, C.A.; Nikolaki, M.D.; Zerva, C.N.; Philippopoulos, C.J.; Pouloupoulos, S.G. Photocatalytic oxidation of benzene, toluene, ethylbenzene and m-xylene in the gas-phase over TiO₂-based catalysts. *J. Photochem. Photobiol. A Chem.* **2012**, *244*, 24–31. [[CrossRef](#)]
16. Al-Sabahi, J.; Bora, T.; Al-Abri, M.; Dutta, J. Efficient visible light photocatalysis of benzene, toluene, ethylbenzene and xylene (BTEX) in aqueous solutions using supported zinc oxide nanorods. *PLoS ONE* **2017**, *12*, e0189276. [[CrossRef](#)] [[PubMed](#)]
17. Tirumala, R.T.A.; Gyawali, S.; Wheeler, A.; Ramakrishnan, S.B.; Sooriyagoda, R.; Mohammadparast, F.; Khatri, N.; Tan, S.; Kalkan, A.K.; Bristow, A.D.; et al. Structure–Property–Performance Relationships of Cuprous Oxide Nanostructures for Dielectric Mie Resonance-Enhanced Photocatalysis. *ACS Catal.* **2022**, *12*, 7975–7985. [[CrossRef](#)]

18. Mohammadparast, F.; Ramakrishnan, S.B.; Khatri, N.; Tirumala, R.T.A.; Tan, S.; Kalkan, A.K.; Andiappan, M. Cuprous Oxide Cubic Particles with Strong and Tunable Mie Resonances for Use as Nanoantennas. *ACS Appl. Nano Mater.* **2020**, *3*, 6806–6815. [[CrossRef](#)]
19. Gyawali, S.; Tirumala, R.T.A.; Loh, H.; Andiappan, M.; Bristow, A.D. Photocatalytic Recombination Dynamics in Highly Scattering Cu₂O Nanocatalyst Clusters. *J. Phys. Chem. C* **2024**, *128*, 2003–2011. [[CrossRef](#)]
20. Dong, Z.; Yang, C.; Zhao, D.; Wang, Y.; Chu, W.; Feng, Z.; Zhu, X.; Xin, W.; Shang, Y.; Liu, S.; et al. Co-Crystalline ZSM-5/ZSM-11 Nanostructures for Alkylation of Benzene with Ethanol. *ACS Appl. Nano Mater.* **2021**, *4*, 10296–10306. [[CrossRef](#)]
21. Mimura, N.; Saito, M. Dehydrogenation of ethylbenzene to styrene over Fe₂O₃/Al₂O₃ catalysts in the presence of carbon dioxide. *Catal. Today* **2000**, *55*, 173–178. [[CrossRef](#)]
22. Shen, Z.; Ma, C.; Wang, D.; He, J.; Sun, H.; Zhu, Z.; Yang, W. Shape-selective alkylation of benzene with ethylene over a core-shell ZSM-5@MCM-41 composite material. *Chin. J. Chem. Eng.* **2021**, *37*, 64–71. [[CrossRef](#)]
23. Yang, W.; Wang, Z.; Sun, H.; Zhang, B. Advances in development and industrial applications of ethylbenzene processes. *Chin. J. Catal.* **2016**, *37*, 16–26. [[CrossRef](#)]
24. Gupta, R.; Uslu, H.; Majumder, S. Production of Styrene from Dehydrogenation of Ethylbenzene. *Chem. Eng. Technol.* **2022**, *45*, 817–823. [[CrossRef](#)]
25. Perego, C.; Ingallina, P. Recent advances in the industrial alkylation of aromatics: New catalysts and new processes. *Catal. Today* **2002**, *73*, 3–22. [[CrossRef](#)]
26. Gao, Y.; Neal, L.; Ding, D.; Wu, W.; Baroi, C.; Gaffney, A.M.; Li, F. Recent Advances in Intensified Ethylene Production—A Review. *ACS Catal.* **2019**, *9*, 8592–8621. [[CrossRef](#)]
27. Zhao, S.; Ma, K.; He, K.; Ma, X.; Dai, C. Direct and Highly Selective One-Step Production of Ethylbenzene from Syngas and Benzene. *Ind. Eng. Chem. Res.* **2023**, *62*, 15834–15843. [[CrossRef](#)]
28. Liu, J.; Xu, H.; Dong, J.; Zhou, L.; Li, X.; Ge, H. Alkylbenzene synthesis from benzene and syngas over a ZnCrO_x/beta bifunctional catalyst. *React. Chem. Eng.* **2022**, *7*, 1447–1460. [[CrossRef](#)]
29. Safi, N.A.; Li, Y.; Yu, B.; Liu, P.; Wang, J.; Ge, H.; Zhang, K. The dependence of high catalytic performance on the tunable oxygen vacancy in the CZ_xS/Zn-HZSM-5 bifunctional catalyst for alkylation of benzene and syngas. *Appl. Organomet. Chem.* **2022**, *36*, e6744. [[CrossRef](#)]
30. Feng, M.; Li, Y.; Liu, P.; Wang, J.; Ge, H.; Zhang, K.; Duan, D.; Wang, L.; Pei, X. A novel alkylation process of benzene with CO₂ and H₂ over bifunctional Zn_xCe_yZr_zO/Z5 catalyst. *Fuel* **2022**, *326*, 125023. [[CrossRef](#)]
31. Zhu, P.; Sun, J.; Yang, G.; Liu, G.; Zhang, P.; Yoneyama, Y.; Tsubaki, N. Tandem catalytic synthesis of benzene from CO₂ and H₂. *Catal. Sci. Technol.* **2017**, *7*, 2695–2699. [[CrossRef](#)]
32. Zuo, J.; Liu, C.; Han, X.; Wen, D.; Liu, X.; Ye, L.; Zhuang, W.; Yuan, Y. Steering CO₂ hydrogenation coupled with benzene alkylation toward ethylbenzene and propylbenzene using a dual-bed catalyst system. *Chem Catal.* **2022**, *2*, 1223–1240. [[CrossRef](#)]
33. Huš, M.; Dasireddy, V.D.B.C.; Strah Štefančič, N.; Likozar, B. Mechanism, kinetics and thermodynamics of carbon dioxide hydrogenation to methanol on Cu/ZnAl₂O₄ spinel-type heterogeneous catalysts. *Appl. Catal. B Environ.* **2017**, *207*, 267–278. [[CrossRef](#)]
34. Zhang, L.; Ji, G.-F.; Zhao, F.; Gong, Z.-Z. First-principles study of the structural, mechanical and electronic properties of ZnX₂O₄ (X=Al, Cr and Ga). *Chin. Phys. B* **2011**, *20*, 047102. [[CrossRef](#)]
35. Vasile, M.; Vlazan, P.; Avram, N.M. Characterization and optical properties of ZnGa₂O₄:Eu³⁺ nanophosphor grown by hydrothermal method. *J. Alloys Compd.* **2010**, *500*, 185–189. [[CrossRef](#)]
36. Liu, X.; Wang, M.; Zhou, C.; Zhou, W.; Cheng, K.; Kang, J.; Zhang, Q.; Deng, W.; Wang, Y. Selective transformation of carbon dioxide into lower olefins with a bifunctional catalyst composed of ZnGa₂O₄ and SAPO-34. *Chem. Commun.* **2018**, *54*, 140–143. [[CrossRef](#)] [[PubMed](#)]
37. Rajkumar, T.; Sapi, A.; Abel, M.; Farkas, F.; Gomez-Perez, J.F.; Kukovecz, A.; Konya, Z. Ni-Zn-Al-Based Oxide/Spinel Nanostructures for High Performance, Methane-Selective CO₂ Hydrogenation Reactions. *Catal. Lett.* **2019**, *150*, 1527–1536. [[CrossRef](#)]
38. Kumar, N.; Kishan, H.; Rao, A.; Awana, V.P.S. Fe ion doping effect on electrical and magnetic properties of La_{0.7}Ca_{0.3}Mn_{1-x}Fe_xO₃ (0 ≤ x ≤ 1). *J. Alloys Compd.* **2010**, *502*, 283–288. [[CrossRef](#)]
39. Yang, F.; Fang, Y.; Liu, X.; Liu, X.; Muir, D.; MacLennan, A.; Zhu, X. One-Step Alkylation of Benzene with Syngas over Non-Noble Catalysts Mixed with Modified HZSM-5. *Ind. Eng. Chem. Res.* **2019**, *58*, 13879–13888. [[CrossRef](#)]
40. Deng, X.; Lu, M.; Meng, J. Effect of heavy doping of nickel in compound Mo₃Sb₇: Structure and thermoelectric properties. *J. Alloys Compd.* **2013**, *577*, 183–188. [[CrossRef](#)]
41. Parthasarathy, S.; Nandhini, V.; Jeyaprakash, B.G. Improved sensing response of photo activated ZnO thin film for hydrogen peroxide detection. *J. Colloid Interface Sci.* **2016**, *482*, 81–88. [[CrossRef](#)] [[PubMed](#)]
42. Gurugubelli, T.R.; Babu, B.; Kim, J.; Yoo, K. Hydrothermal synthesis of Fe-doped ZnAl₂O₄ nanosheets: Bandgap engineering and room temperature ferromagnetism. *Chem. Pap.* **2021**, *75*, 6407–6416. [[CrossRef](#)]
43. Akika, F.Z.; Benamira, M.; Lahmar, H.; Trari, M.; Avramova, I.; Suzer, S. Structural and optical properties of Cu-doped ZnAl₂O₄ and its application as photocatalyst for Cr(VI) reduction under sunlight. *Surf. Interfaces* **2020**, *18*, 100406. [[CrossRef](#)]
44. Zhang, P.; Ma, L.; Meng, F.; Wang, L.; Zhang, R.; Yang, G.; Li, Z. Boosting CO₂ hydrogenation performance for light olefin synthesis over GaZrO_x combined with SAPO-34. *Appl. Catal. B Environ.* **2022**, *305*, 121042. [[CrossRef](#)]

45. Chen, J.-X.; Li, X.-X.; Ma, H.-P.; Huang, W.; Ji, Z.-G.; Xia, C.; Lu, H.-L.; Zhang, D.W. Investigation of the Mechanism for Ohmic Contact Formation in Ti/Al/Ni/Au Contacts to β -Ga₂O₃ Nanobelt Field-Effect Transistors. *ACS Appl. Mater. Interfaces* **2019**, *11*, 32127–32134. [[CrossRef](#)] [[PubMed](#)]
46. Ito, R.; Akatsuka, M.; Ozawa, A.; Kato, Y.; Kawaguchi, Y.; Yamamoto, M.; Tanabe, T.; Yoshida, T. Photocatalytic Activity of Ga₂O₃ Supported on Al₂O₃ for Water Splitting and CO₂ Reduction. *ACS Omega* **2019**, *4*, 5451–5458. [[CrossRef](#)] [[PubMed](#)]
47. Zhao, Y.; Cheng, J.; Zhang, P.; Liu, X.; Zhuang, J.; Yu, Y.; Zhao, Q.; Wang, Y.; Zhu, X.; Yang, F. Examination of key factors determining the catalytic performance of Zn-Ga/HZSM-5 bifunctional catalysts and establishment of reaction network in alkylation of benzene with carbon dioxide. *Appl. Catal. A Gen.* **2022**, *643*, 118785. [[CrossRef](#)]
48. Fu, L.; Liu, Y.; Hu, P.; Xiao, K.; Yu, G.; Zhu, D. Ga₂O₃ Nanoribbons: Synthesis, Characterization, and Electronic Properties. *Chem. Mater.* **2003**, *15*, 4287–4291. [[CrossRef](#)]
49. Gao, P.; Dang, S.; Li, S.; Bu, X.; Liu, Z.; Qiu, M.; Yang, C.; Wang, H.; Zhong, L.; Han, Y.; et al. Direct Production of Lower Olefins from CO₂ Conversion via Bifunctional Catalysis. *ACS Catal.* **2018**, *8*, 571–578. [[CrossRef](#)]
50. Sood, A.; Tarntair, F.-G.; Wang, Y.-X.; Chang, T.-C.; Chen, Y.-H.; Liu, P.-L.; Horng, R.-H. Performance enhancement of ZnGa₂O₄ Schottky type deep-ultraviolet photodetectors by oxygen supercritical fluid treatment. *Results Phys.* **2021**, *29*, 104764. [[CrossRef](#)]
51. He, H.; Lin, X.; Li, S.; Wu, Z.; Gao, J.; Wu, J.; Wen, W.; Ye, D.; Fu, M. The key surface species and oxygen vacancies in MnO_x(0.4)-CeO₂ toward repeated soot oxidation. *Appl. Catal. B Environ.* **2018**, *223*, 134–142. [[CrossRef](#)]
52. Wang, S.; Wang, P.; Shi, D.; He, S.; Zhang, L.; Yan, W.; Qin, Z.; Li, J.; Dong, M.; Wang, J.; et al. Direct Conversion of Syngas into Light Olefins with Low CO₂ Emission. *ACS Catal.* **2020**, *10*, 2046–2059. [[CrossRef](#)]
53. Jiang, F.; Wang, S.; Liu, B.; Liu, J.; Wang, L.; Xiao, Y.; Xu, Y.; Liu, X. Insights into the Influence of CeO₂ Crystal Facet on CO₂ Hydrogenation to Methanol over Pd/CeO₂ Catalysts. *ACS Catal.* **2020**, *10*, 11493–11509. [[CrossRef](#)]
54. Wang, W.; Seiler, M.; Hunger, M. Role of Surface Methoxy Species in the Conversion of Methanol to Dimethyl Ether on Acidic Zeolites Investigated by in Situ Stopped-Flow MAS NMR Spectroscopy. *J. Phys. Chem. B* **2001**, *105*, 12553–12558. [[CrossRef](#)]
55. Shen, C.; Bao, Q.; Xue, W.; Sun, K.; Zhang, Z.; Jia, X.; Mei, D.; Liu, C.-j. Synergistic effect of the metal-support interaction and interfacial oxygen vacancy for CO₂ hydrogenation to methanol over Ni/In₂O₃ catalyst: A theoretical study. *J. Energy Chem.* **2022**, *65*, 623–629. [[CrossRef](#)]
56. Ghavipour, M.; Al Hussami, R.; Levin, K.; Roy, R.; Kopyscinski, J. SAPO-34 Catalyst: Synthesis Optimization by Template Alteration and In Situ Coke Evolution Analysis in Methanol Conversion to Light Olefins. *Ind. Eng. Chem. Res.* **2023**, *62*, 18362–18378. [[CrossRef](#)]
57. Huang, Y.; Ma, H.; Xu, Z.; Qian, W.; Zhang, H.; Ying, W. Role of nanosized sheet-like SAPO-34 in bifunctional catalyst for syngas-to-olefins reaction. *Fuel* **2020**, *273*, 117771. [[CrossRef](#)]
58. Choi, S.-W.; Kim, W.-G.; So, J.-S.; Moore, J.S.; Liu, Y.; Dixit, R.S.; Pendergast, J.G.; Sievers, C.; Sholl, D.S.; Nair, S.; et al. Propane dehydrogenation catalyzed by gallosilicate MFI zeolites with perturbed acidity. *J. Catal.* **2017**, *345*, 113–123. [[CrossRef](#)]
59. Nan, Y.; Ma, S.; Zha, F.; Tian, H.; Tang, X.; Chang, Y.; Guo, X. Facile surfactant-assisted synthesis of nanosheet-like mesoporous SAPO-34 zeolites and catalysis performance for methanol to olefins. *React. Kinet. Mech. Catal.* **2022**, *135*, 1987–1998. [[CrossRef](#)]
60. Yang, F.; Zhong, J.; Liu, X.; Zhu, X. A novel catalytic alkylation process of syngas with benzene over the cerium modified platinum supported on HZSM-5 zeolite. *Appl. Energy* **2018**, *226*, 22–30. [[CrossRef](#)]
61. Potter, M.E.; Kezina, J.; Bounds, R.; Carravetta, M.; Mezza, T.M.; Raja, R. Investigating the role of framework topology and accessible active sites in silicoaluminophosphates for modulating acid-catalysis. *Catal. Sci. Technol.* **2018**, *8*, 5155–5164. [[CrossRef](#)]
62. Yang, F.; Zhou, Q.; Wang, J.; Ding, H.; Zhu, X.; Zhu, K.; Fan, W. Conquering the solubility barrier of di-n-octylamine as structure-directing agent in hierarchical silicoaluminophosphate synthesis by using phase-transfer synthesis. *Chem. Eng. J.* **2023**, *461*, 141887. [[CrossRef](#)]
63. Yu, G.; Chen, X.; Xue, W.; Ge, L.; Wang, T.; Qiu, M.; Wei, W.; Gao, P.; Sun, Y. Melting-assisted solvent-free synthesis of SAPO-11 for improving the hydroisomerization performance of n-dodecane. *Chin. J. Catal.* **2020**, *41*, 622–630. [[CrossRef](#)]
64. Bai, Y.; Yang, F.; Liu, X.; Liu, C.; Zhu, X. Performance of Bifunctional ZnZr/ZSM-5 Catalysts in the Alkylation of Benzene with Syngas. *Catal. Lett.* **2018**, *148*, 3618–3627. [[CrossRef](#)]
65. Han, F.; Liu, H.; Cheng, W.; Xu, Q. Highly selective conversion of CO₂ to methanol on the CuZnO-ZrO₂ solid solution with the assistance of plasma. *RSC Adv.* **2020**, *10*, 33620–33627. [[CrossRef](#)] [[PubMed](#)]
66. Niu, J.; Zhang, C.; Liu, H.; Jin, Y.; Zhang, R. Enhanced performance of oxygen vacancies on CO₂ adsorption and activation over different phases of ZrO₂. *Front. Energy* **2023**, *17*, 545–554. [[CrossRef](#)]
67. Ye, J.; Liu, C.; Mei, D.; Ge, Q. Active Oxygen Vacancy Site for Methanol Synthesis from CO₂ Hydrogenation on In₂O₃(110): A DFT Study. *ACS Catal.* **2013**, *3*, 1296–1306. [[CrossRef](#)]
68. Dahl, I.M.; Kolboe, S. On the reaction mechanism for propene formation in the MTO reaction over SAPO-34. *Catal. Lett.* **1993**, *20*, 329–336. [[CrossRef](#)]
69. Tao, S.; Zhang, X.; Li, X.; Wang, Y.; Wang, B.; Yuan, Y.; Zhang, D.; Du, S.; Li, X. Hierarchical low-silica SAPO-34 with enhanced MTO performance: Mesopore template- and fluoride-free synthesis. *Microporous Mesoporous Mater.* **2023**, *349*, 112425. [[CrossRef](#)]

70. Tian, P.; Wei, Y.; Ye, M.; Liu, Z. Methanol to Olefins (MTO): From Fundamentals to Commercialization. *ACS Catal.* **2015**, *5*, 1922–1938. [[CrossRef](#)]
71. Emeis, C.A. Determination of Integrated Molar Extinction Coefficients for Infrared Absorption Bands of Pyridine Adsorbed on Solid Acid Catalysts. *J. Catal.* **1993**, *141*, 347–354. [[CrossRef](#)]

Disclaimer/Publisher’s Note: The statements, opinions and data contained in all publications are solely those of the individual author(s) and contributor(s) and not of MDPI and/or the editor(s). MDPI and/or the editor(s) disclaim responsibility for any injury to people or property resulting from any ideas, methods, instructions or products referred to in the content.